eMicrobe
https://www.sciltp.com/journals/emicrobe

Article

Structural and Energetic Characterization of the TmGpx1–CK2β Complex Using Molecular Dynamics Simulations

Yin Htet Htet Oo [1], Tanaporn Wangsanut [1], Narin Lawan [2] and Monsicha Pongpom [1,*]

[1] Department of Microbiology, Faculty of Medicine, Chiang Mai University, Chiang Mai 50200, Thailand
[2] Department of Chemistry, Faculty of Science, Chiang Mai University, Chiang Mai 50200, Thailand
* Correspondence: monsicha.p@cmu.ac.th

How To Cite: Oo, Y.H.H.; Wangsanut, T.; Lawan, N.; et al. Structural and Energetic Characterization of the TmGpx1–CK2β Complex Using Molecular Dynamics Simulations. *eMicrobe* **2026**, *2*(4), 17. https://doi.org/10.53941/emicrobe.2026.100017

Received: 1 August 2026
Revised: 20 August 2026
Accepted: 8 October 2026
Published: 19 October 2026

Abstract: *Talaromyces marneffei* is a dimorphic fungal pathogen that survives within host macrophages by counteracting oxidative and immune stress. Recently, several host macrophage proteins interacting with the antigenic *T. marneffei* glutathione peroxidase TmGpx1 were identified. Among these candidate proteins, the regulatory subunit of casein kinase 2, CK2β (CSNK2B), was selected for structural modeling and molecular dynamics simulations to investigate the molecular basis of the host-pathogen interaction. Our findings also suggest a previously unrecognized role for fungal glutathione peroxidase in modulating host cytoskeleton regulation. Here, we used an AlphaFold3-based structure prediction and molecular dynamics simulations to characterize and evaluate the TmGpx1–CK2β interaction. The complex remained stably associated throughout the 200 ns simulations, with sustained intermolecular proximity, extensive heavy-atom contacts, and a persistent hydrogen-bond network. MM/GBSA calculations indicated a favorable total binding energy (−58.17 ± 13.13 kcal/mol), driven mainly by van der Waals and electrostatic contributions. Two contact pairs, TmGpx1 Arg128–CK2β Trp12 and TmGpx1 Val126–CK2β Glu73, were conserved across all three replicates and coincided with the residues contributing most favorably to binding energy. Notably, TmGpx1 Leu123, Leu124, and Val126—residues previously implicated in the TmGpx1–FKBP15 interaction—recurred at the CK2β interface, and the TmGpx1 catalytic triad (Cys39, Gln76, Trp131) was also engaged in CK2β binding. These findings support a stable and energetically favorable TmGpx1–CK2β interface and suggest that TmGpx1 recognizes multiple host regulatory proteins through a shared interaction surface that may be functionally linked to its catalytic activity.

Keywords: *Talaromyces marneffei*; TmGpx1; glutathione peroxidase; CK2β (CSNK2B); molecular dynamics simulation; protein–protein interaction; moonlighting protein; host–pathogen interaction

1. Introduction

Talaromycosis, caused by the thermally dimorphic fungal pathogen *Talaromyces marneffei*, remains a life-threatening endemic mycosis in Southeast Asia, with mortality approaching one-third of affected individuals [1,2]. A central feature of *T. marneffei* pathogenesis is its temperature-dependent morphological transition. The fungus grows as a mold at 25 °C but converts to a pathogenic yeast form at 37 °C after uptake by host macrophages, where it can survive and replicate intracellularly while being protected from neutrophil-mediated clearance [3–5]. Adaptation to this hostile intracellular environment requires coordinated stress-response mechanisms, including heat-shock proteins that support thermally regulated morphogenesis [6], aspartyl proteases that promote growth

Copyright: © 2026 by the authors. This is an open access article under the terms and conditions of the Creative Commons Attribution (CC BY) license (https://creativecommons.org/licenses/by/4.0/).
Publisher's Note: Scilight stays neutral with regard to jurisdictional claims in published maps and institutional affiliations.

within phagocytes [7], and antioxidant systems that protect the fungus from host-derived reactive oxygen species. Among these defenses, the glutathione antioxidant system contributes to redox homeostasis through glutathione peroxidase-catalyzed reduction of hydrogen peroxide and other hydroperoxides [8].

Glutathione peroxidase of *T. marneffei* (TmGpx1) was previously identified as an antigenic protein recognized by antibodies from patients with talaromycosis, indicating its exposure to the host immune system during infection [9,10]. Proteomic studies have also detected TmGpx1 in extracellular vesicles released by *T. marneffei*, despite the absence of a classical secretion signal [11]. This extracellular localization is difficult to reconcile with an exclusively cytosolic antioxidant role and raises the possibility that TmGpx1 may perform additional functions after being transported outside the fungal cell. Such behavior is consistent with protein moonlighting, in which a single protein performs multiple mechanistically distinct functions depending on its localization, cellular environment, or interaction partners [12,13].

To investigate the potential host-interacting role of TmGpx1, we previously performed a yeast two-hybrid screen using full-length TmGpx1 as bait against a cDNA library derived from non-induced human macrophages [14]. Protein candidate human interaction partners were identified, several of which are associated with cytoskeletal organization, membrane trafficking, and extracellular vesicle-related processes. One candidate, FK506-binding protein 15 (FKBP15), is involved in cytoskeletal coordination and early endosomal trafficking. The Y2H-supported TmGpx1–FKBP15 interaction was subsequently examined using molecular dynamics simulation and MM/GBSA analysis, which demonstrated a persistent and energetically favorable association within the sampled trajectories and identified candidate interface residues [14]. These findings provided initial structural support for a possible host-interacting function of TmGpx1 beyond its canonical antioxidant activity.

Among the candidate host partners recovered from the TmGpx1 Y2H screen was casein kinase 2 beta subunit (CK2β; CSNK2B), the regulatory subunit of casein kinase 2 (CK2) [14]. CK2 is a highly conserved, constitutively active serine/threonine kinase involved in proliferation, survival, transcription, DNA repair, and cytoskeletal organization, and is assembled as a heterotetramer of two catalytic subunits (CK2α and/or CK2α′) and a dimer of two CK2β regulatory subunits. CK2β itself has no intrinsic kinase activity; instead, it functions as a regulatory docking platform that governs holoenzyme assembly, substrate recruitment, and interaction specificity, such that binding of an external protein to CK2β can potentially redirect CK2 activity without engaging the catalytic subunits directly [15,16].

CK2 signaling—including a non-redundant contribution from CK2β itself—is closely linked to actin and microtubule cytoskeletal organization across organisms from yeast to mammals [17–20]. This cytoskeletal role is particularly relevant in macrophages, where actin and microtubule remodeling underlies phagocytosis, phagosome maturation, and intracellular pathogen clearance, and where CK2 signaling has also been implicated in innate immune and antimicrobial responses [21]. The Y2H-supported association between TmGpx1 and CK2β therefore raises the possibility that TmGpx1 engages a host regulatory scaffold connected to both kinase signaling and cytoskeletal organization, potentially affecting CK2β-dependent partner recruitment or cytoskeletal regulation; however, this has not yet been experimentally established.

Although Y2H screening provides evidence that two proteins can associate, it does not define the molecular interface, conformational behavior, or energetic characteristics of the interaction. It therefore remains unclear whether the TmGpx1–CK2β pair can maintain a persistent interface under dynamic, solvated conditions and which residues contribute to the proposed association. In the present study, molecular dynamics simulations were used to characterize the structural behavior of the predicted TmGpx1–CK2β complex across independent trajectories. Global conformational dynamics, intermolecular distances, atomic contacts, hydrogen bonds, salt bridges, buried surface area, conformational clustering, and MM/PBSA and MM/GBSA binding-energy estimates were evaluated. This study aimed to assess the structural plausibility of the Y2H-supported interaction and identify recurrent interface residues that may be prioritized for future biochemical and cellular validation.

2. Materials and Methods

2.1. Sequence Retrieval and Structural Prediction

The amino acid sequences of glutathione peroxidase 1 from *Talaromyces marneffei* ATCC 18224 (TmGpx1/Hyr1; NCBI accession EEA19957.1; 197 amino acids) and human casein kinase II subunit beta (CK2β /CSNK2B; NCBI accession NP_001311.3; 215 amino acids) were retrieved from the NCBI Protein database in FASTA format (accessed on 24 March 2026). The full-length sequences of CK2 were submitted as a heterodimeric complex to the AlphaFold Server (accessed on 11 May 2026), powered by AlphaFold 3 model [22,23]. The generated models were evaluated based on the overall ranking score, predicted template modeling score (pTM), interface predicted template modeling score (ipTM), predicted fraction of disordered residues, and the presence of

structural clashes. Model 0 was selected as the first-ranked output among the models with the highest confidence metrics and was used as the starting structure for molecular dynamics simulation. The amino acid sequences used for structural prediction and the confidence metrics of the generated models are provided in Supplementary Data 1 and 2, respectively.

2.2. Molecular Dynamics Simulations

MD simulations were performed using the GROMACS software package (version 2022.4) on the CMU HPC ERAWAN system (Information Technology Service Center, Chiang Mai University), comprising CPU nodes equipped with AMD EPYC 7742 (64 cores × 2 per node, 2.25 GHz) and AMD EPYC 9534 (64 cores × 2 per node, 2.45 GHz), and GPU nodes equipped with NVIDIA A100 80 GB and NVIDIA H100 80 GB GPUs. Each SLURM job requested 4 CPU cores and 1 GPU, with node assignment determined by resource availability at job submission.

The AlphaFold3-predicted TmGpx1–CK2β complex was converted into a GROMACS-compatible topology using the gmx pdb2gmx module, with the AMBER99SB force field and the TIP3P three-point water model applied. The complex was placed at the center of a cubic simulation box with a minimum solute–boundary distance of 1.0 nm using gmx editconf, and the box was solvated with TIP3P water using gmx solvate. The system was neutralized by the addition of Na^+ and Cl^- counterions sufficient to offset the net protein charge, using gmx genion following system preprocessing with gmx grompp.

Energy minimization was performed using the steepest descent algorithm, with a maximum force tolerance of 1000.0 kJ/mol/nm and a maximum of 50,000 steps. Short-range electrostatic and van der Waals interactions were truncated at 1.0 nm, with long-range electrostatics treated by the particle mesh Ewald (PME) method. Following minimization, the system was equilibrated in two sequential phases, each performed for 100 ps (50,000 steps, 2 fs timestep) with position restraints applied to the protein. In the constant-volume, constant-temperature (NVT) phase, temperature was maintained at 310.15 K using the V-rescale thermostat (coupling time constant τ = 0.1 ps) applied separately to protein and solvent/ion groups. In the constant-pressure, constant-NPT phase, pressure was additionally maintained at 1.0 bar using the Parrinello–Rahman barostat (isotropic coupling, τ = 2.0 ps, compressibility = 4.5×10^{-5} bar^{-1}), while temperature coupling was continued as in the NVT phase. Bonds involving hydrogen atoms were constrained using the LINCS algorithm in both equilibration phases.

Production MD simulations were performed for 200 ns per replicate (100,000,000 steps, 2 fs timestep) across three independent replicates, using the leapfrog integrator. Temperature and pressure were maintained as in the NPT equilibration (V-rescale thermostat, 310.15 K; Parrinello–Rahman barostat, 1.0 bar), and LINCS constraints were retained for hydrogen-containing bonds. Long-range electrostatics were computed using PME, with short-range electrostatic and van der Waals cutoffs of 1.0 nm. Trajectory coordinates were saved every 10 ps. Production runs exceeding the cluster's per-job wall time limit were resumed using gmx convert-tpr to extend the simulation, followed by gmx mdrun with the -cpi flag to continue from the last checkpoint file.

2.3. Trajectory Analysis

Concatenated and centered trajectories were used for all subsequent analyses. Unless otherwise noted, analyses were performed over the full 200 ns production trajectory for each of the three independent replicates. Backbone RMSD of the TmGpx1–CK2β complex, and of each protein individually, was calculated relative to the initial structure using gmx rms. Per-residue RMSF was calculated using gmx rmsf to assess local structural flexibility. The radius of gyration (Rg) of the complex was calculated using gmx gyrate to monitor overall compactness over time.[24] Statistical calculations: unless otherwise stated, overall values reported in the Results section are the mean ± SD calculated from the three independent replicate-level means, while the trajectory mean ± temporal SD for each individual 200-ns simulation is provided in Supplementary Tables S1 and S2.

The minimum intermolecular distance between TmGpx1 and CK2β was monitored using gmx mindist. Interfacial heavy-atom contacts were quantified using gmx mindist with a 0.45 nm distance cutoff, generating a time-resolved count of atom pairs within this threshold across the full trajectory. Intermolecular hydrogen bonds were identified using gmx hbond, applying a donor–acceptor distance cutoff of 0.35 nm and a hydrogen-bond angle cutoff of 45°. Hydrogen bond occupancy for individual donor–acceptor pairs was calculated as the percentage of trajectory frames in which a given pair was hydrogen-bonded, determined from the gmx hbond existence map output.

Salt bridges were identified between oppositely charged side-chain atoms of the two proteins: positively charged groups were defined as the lysine amino nitrogen (NZ), arginine guanidinium nitrogens (NE, NH1, NH2), and protonated histidine imidazole nitrogens (ND1, NE2), while negatively charged groups were defined as the

aspartate and glutamate carboxylate oxygens (OD1/OD2 and OE1/OE2, respectively). Salt bridges between TmGpx1 and CK2β were identified using gmx mindist, applying a 0.40 nm distance cutoff between the charged atom groups. Both charge pairings were analyzed—TmGpx1 negative against CK2β positive, and the reciprocal TmGpx1 positive against CK2β negative—to capture all possible interfacial salt bridges. Solvent-accessible surface area (SASA) was calculated for CK2β alone, TmGpx1 alone, and the TmGpx1–CK2β complex using gmx sasa. The buried surface area (BSA) was calculated for each trajectory frame as BSA = SASA(CK2β) + SASA(TmGpx1)–SASA (complex).

Representative complex conformations were identified by clustering the final 50 ns (150–200 ns window; 5001 frames) of each replicate trajectory using the GROMOS algorithm implemented in gmx cluster, with an RMSD cutoff of 0.50 nm. The most populated cluster (Cluster 1) was selected as the representative structure for structural figures and per-residue interaction analysis in each replicate. Interfacial residue–residue contact pairs were identified using a custom MDAnalysis-based script employing the capped_distance function, applying a 0.60 nm heavy-atom distance cutoff. Contact frequency for each residue pair was calculated as the percentage of trajectory frames in which the pair was in contact, and pairs with a contact frequency ≥30% were retained for reporting. Binding free energies between TmGpx1 and CK2β were calculated using both the Molecular Mechanics Generalized Born Surface Area (MM-GBSA; igb = 5, salt concentration 0.15 M) implemented in the gmx_MMPBSA package (version 1.6.4) [25]. Calculations were performed across the full 0–200 ns trajectory of each replicate, sampled at 1 ns interval (201 frames total). Per-residue energy decomposition was performed for residues within 4 Å of the interface, and residue-level ΔG contributions were merged with the interfacial contact pair data described above.

3. Results

3.1. Structural Evolution of the TmGpx1–CK2β Complex

The structural evolution of the TmGpx1–CK2β complex was examined across three independent 200-ns molecular dynamics simulations. Representative structures extracted at 0, 100, and 200 ns showed progressive conformational rearrangement relative to the predicted starting structure (Figure 1). Superimposition of the initial and final structures indicated that the largest displacements occurred in terminal and loop regions, whereas the principal folded regions of CK2β and TmGpx1 remained intact and the two proteins remained associated.

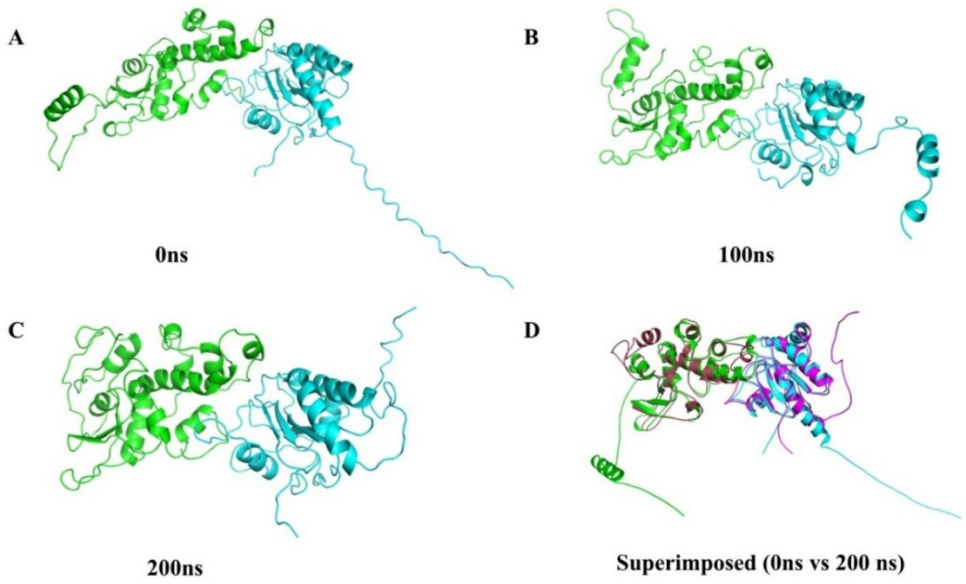


Figure 1. Structural evolution and superimposition of the TmGpx1–CK2β complex during molecular dynamics simulation. (**A**–**C**) Snapshots at 0, 100, and 200 ns show the complex in cartoon representation, with CK2β in green (chain A) and TmGpx1 in cyan (chain B); progressive rearrangements are apparent in loop regions and interfacial contacts over the trajectory. (**D**) Superimposition of the initial and final conformations, with the initial structure shown in green (CK2β, chain A) and cyan (TmGpx1, chain B), and the final (200 ns) structure shown in raspberry (CK2β, chain A) and magenta (TmGpx1, chain B). Core regions remain stable across the overlay, while localized flexibility persists at the interface, reflecting dynamic adaptation during the simulation.

3.2. The Complex Remains Compact Despite Conformational Rearrangement

The complete TmGpx1–CK2β complex showed an overall backbone RMSD of 1.414 ± 0.195 nm across the three replicate-level means (Figure 2A; Supplementary Table S1). Although the RMSD increased relative to the initial predicted structure, the radius of gyration decreased during the early simulation period and subsequently remained within a compact range, with an overall mean of 2.836 ± 0.098 nm (Figure 2B). These findings indicate that the complex underwent conformational rearrangement without progressive expansion or global unfolding.

When the proteins were fitted individually, CK2β and TmGpx1 showed overall backbone RMSD values of 1.087 ± 0.126 and 1.230 ± 0.148 nm, respectively (Figure 2C,D). TmGpx1 therefore showed a slightly higher replicate-averaged deviation and broader trajectory fluctuations than CK2β. The individual radius-of-gyration profiles supported maintenance of the folded architectures of both proteins, with overall means of 1.989 ± 0.053 nm for CK2β and 1.919 ± 0.077 nm for TmGpx1 (Supplementary Figure S1 and Table S1).

The Cα RMSF profiles showed that most residues within the folded regions of both proteins had relatively low fluctuations (Figure 2E,F). Increased mobility was concentrated mainly in terminal regions. CK2β exhibited elevated flexibility within its C-terminal segment, most prominently in Replicates 1 and 3, whereas TmGpx1 showed a pronounced increase in fluctuation near its C-terminus, particularly in Replicate 2.

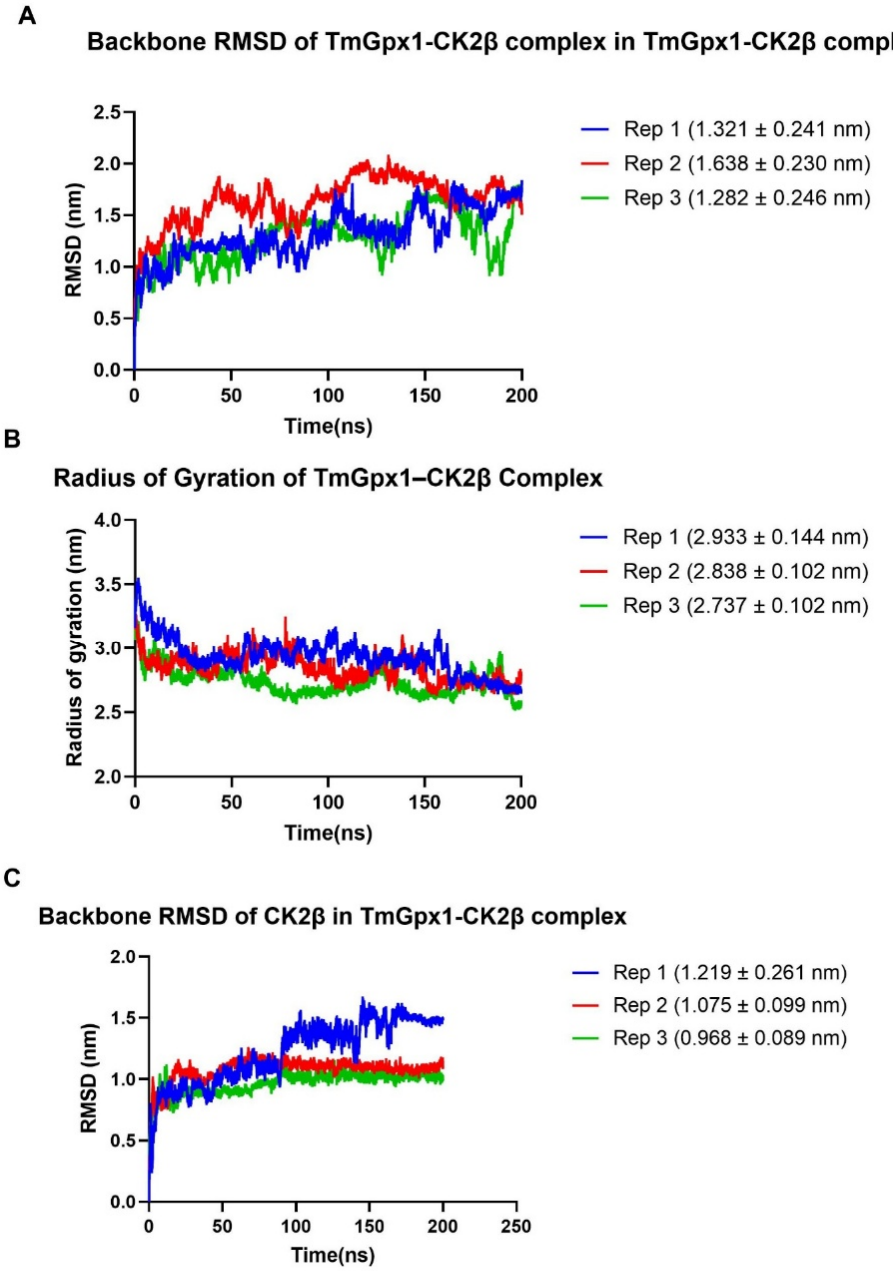


Figure 2. *Cont.*

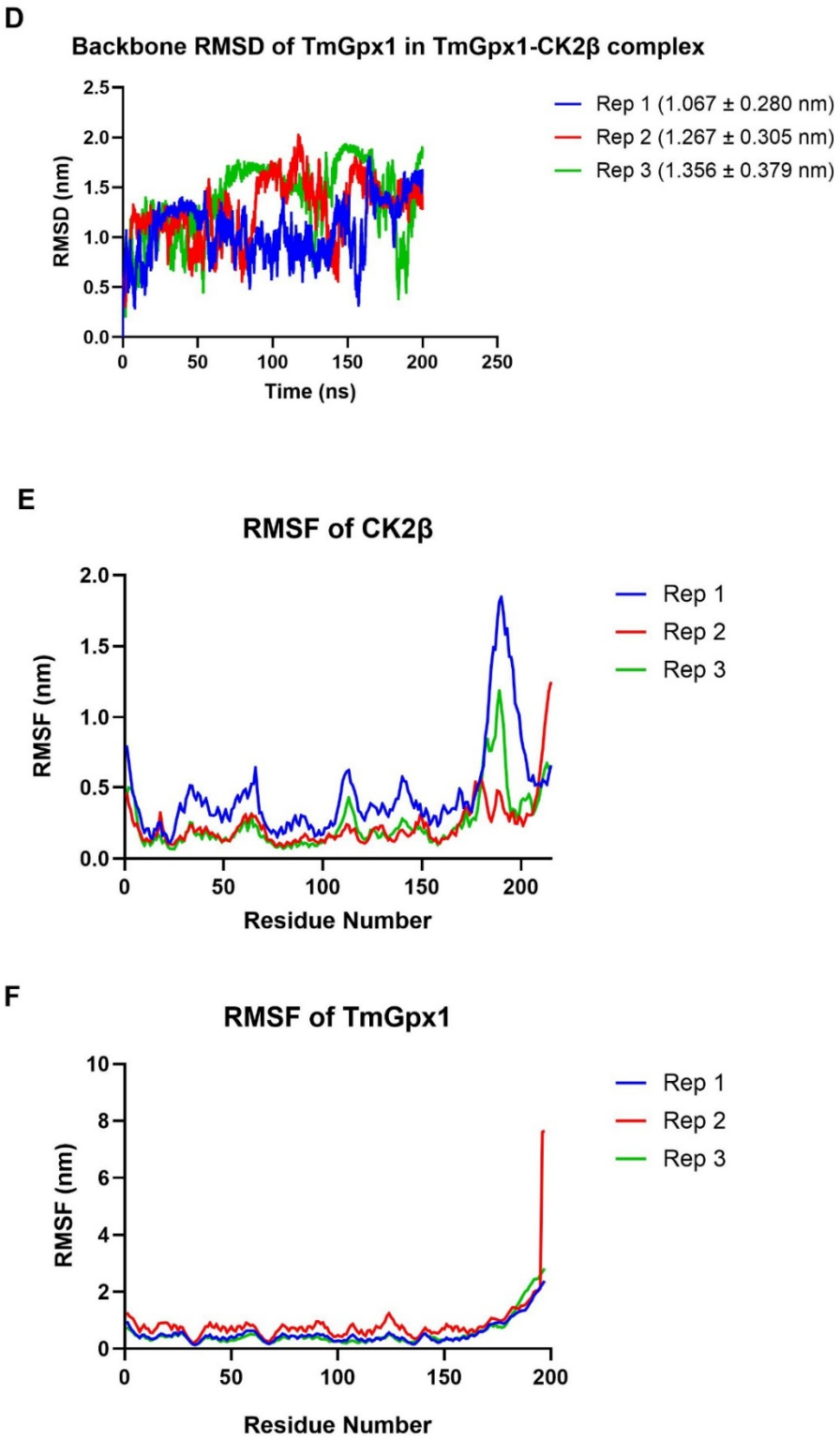


Figure 2. Structural stability and residue-level flexibility of the TmGpx1–CK2β complex during molecular dynamics simulations. Three independent 200-ns simulations were performed, with Replicates 1, 2, and 3 shown in blue, red, and green, respectively. (**A**) Backbone root-mean-square deviation (RMSD) of the complete TmGpx1–CK2β complex relative to the reference structure. (**B**) Radius of gyration (Rg) of the complex, reflecting changes in its overall compactness. (**C**,**D**) Backbone RMSD calculated separately for CK2β and TmGpx1, respectively. (**E**,**F**) Residue-wise Cα root-mean-square fluctuation (RMSF) profiles of CK2β and TmGpx1, respectively. The values displayed in the legends of panels **A**–**D** represent the time-averaged mean ± SD calculated over the corresponding simulation trajectory.

3.3. TmGpx1 and CK2β Maintain a Persistent Molecular Interface

The minimum intermolecular distance remained consistently short throughout the simulations, with an overall mean of 0.266 ± 0.001 nm and no sustained separation event in any replicate (Figure 3A; Supplementary Table S1). The interface maintained an average of 213.8 ± 43.8 heavy-atom contacts using a 0.45-nm cutoff (Figure 3B; Supplementary Table S1). Replicate 3 contained fewer contacts than Replicates 1 and 2 but retained continuous intermolecular association.

The complex maintained 11.74 ± 0.28 intermolecular hydrogen bonds per frame across the three replicate-level means (Figure 3C; Supplementary Table S1). Hydrogen-bond occupancy analysis showed that the specific donor–acceptor network varied among simulations (Supplementary Table S3). The highest-occupancy interactions were (Gly40) TmGpx1—(Glu57) CK2β in Replicate 1 (46.39%), (Lys117) TmGpx1—(Glu5) CK2β in Replicate 2 (65.63%), and (Leu130) TmGpx1—(Trp12) CK2β in Replicate 3 (96.50%). Replicate 3 also contained a persistent hydrogen bond involving (Leu124) TmGpx1—(Ser69) CK2β (72.93%) and Replicate 2 contained a hydrogen bond involving (Leu123) TmGpx1—(Arg17) CK2β (36.32%); both residues are discussed further below in relation to the contact-analysis results. An additional recurring hydrogen bond, (Gln76) TmGpx1—(Glu57) CK2β, was observed in both Replicate 1 (up to 43.81%) and Replicate 2 (up to 30.79%). Thus, the polar interaction network reorganized among replicates while maintaining a similar overall number of hydrogen bonds.

The buried surface area remained nonzero throughout all trajectories, with an overall mean of 18.60 ± 1.56 nm² (Figure 3D). The solvent-accessible surface area of the complex decreased during the initial simulation period and then fluctuated within a relatively consistent range for the complete complex, CK2β, and TmGpx1 individually (Supplementary Figure S2 and Table S2). These findings support initial structural compaction followed by maintenance of a solvent-buried interface.

Salt-bridge analysis revealed pronounced directional asymmetry (Supplementary Figure S3). Contacts between positively charged TmGpx1 residues and negatively charged CK2β residues occurred at an overall minimum distance of 0.272 ± 0.001 nm, with 6.84 ± 1.08 contacts per frame. In contrast, negatively charged TmGpx1 residues and positively charged CK2β residues were separated by a greater mean distance of 1.192 ± 0.536 nm and formed only 0.317 ± 0.539 contacts per frame. Therefore, interfacial electrostatic complementarity was oriented predominantly from basic TmGpx1 residues toward acidic CK2β residues.

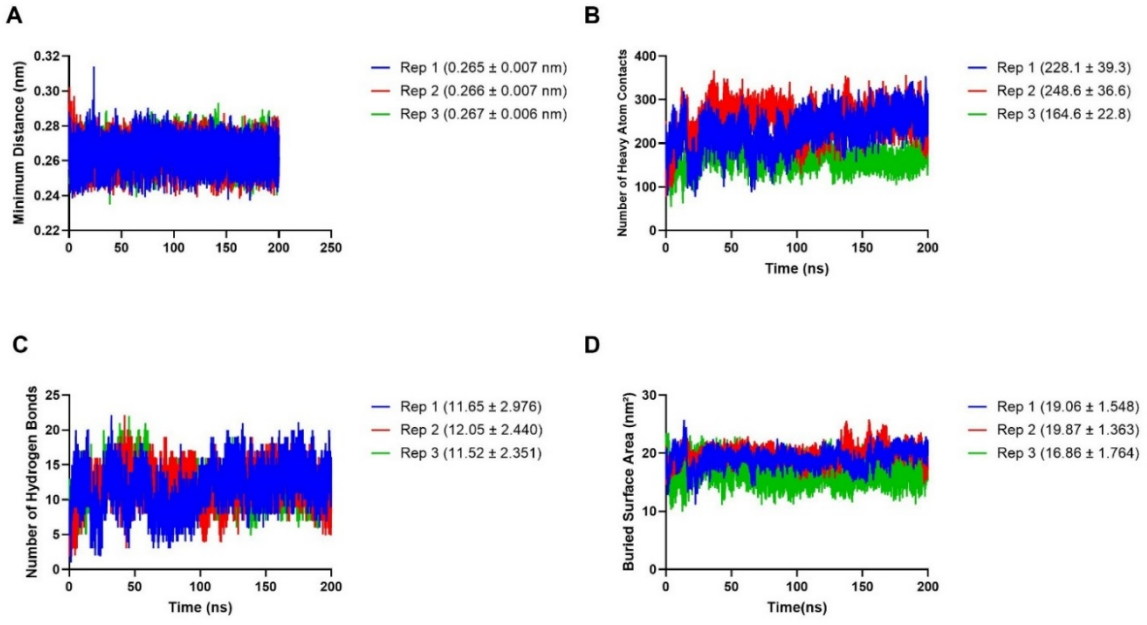


Figure 3. Intermolecular contact and interface stability of the TmGpx1–CK2β complex during molecular dynamics simulations. Three independent 200-ns simulations are shown for Replicate 1 (blue), Replicate 2 (red), and Replicate 3 (green). (**A**) Minimum distance between TmGpx1 and CK2β heavy atoms throughout the simulations. (**B**) Number of intermolecular heavy-atom contacts between TmGpx1 and CK2β, calculated using a 0.45-nm distance cutoff. (**C**) Number of intermolecular hydrogen bonds formed between the two proteins. (**D**) Buried surface area at the TmGpx1–CK2β interface, calculated from the solvent-accessible surface areas of the individual proteins and the complex. Values shown in the legends represent the time-averaged mean ± SD for each trajectory.

3.4. Conformational Clustering Identifies Dominant Bound States

RMSD-based clustering of the final 50 ns of each simulation using the GROMOS algorithm with a 0.50-nm cutoff identified 11, 12, and 7 clusters in Replicates 1, 2, and 3, respectively (Supplementary Table S4). The dominant cluster represented 65.91%, 65.89%, and 55.71% of the sampled conformations, respectively. The three most populated clusters collectively accounted for 89.46%, 92.58%, and 87.80% of frames, indicating that most conformations were concentrated within a limited number of dominant bound states. The complete cluster distributions are provided in Supplementary Table S5.

3.5. MM/GBSA Calculations Support Favorable Complex Formation

MM/GBSA calculations produced negative total binding energies in all three simulations, with values of −63.06, −68.16, and −43.30 kcal/mol for Replicates 1, 2, and 3, respectively. The overall total binding energy was −58.17 ± 13.13 kcal/mol (Table 1).

Table 1. MM/GBSA-derived binding free-energy components for the TmGpx1–CK2β complex across three replicates. Values are reported in kcal/mol as individual replicate results and mean ± SD.

MM/GBSA Model	Rep1	Rep2	Rep3	Mean ± SD (kcal/mol)
ΔVDWAALS	−70.36	−80.25	−58.32	−69.64 ± 10.98
ΔEEL	−1147.21	−1098.92	−766.29	−1004.14 ± 207.39
ΔEGB	1165.28	1123.27	790.24	1026.26 ± 205.48
ΔESURF	−10.76	−12.26	−8.93	−10.65 ± 1.67
ΔGGAS	−1217.57	−1179.17	−824.61	−1073.78 ± 216.64
ΔGSOLV	1154.51	1111.01	781.30	1015.61 ± 204.08
ΔTOTAL	**−63.06**	**−68.16**	**−43.30**	**−58.17 ± 13.13**

Abbreviations: MM/GBSA, Molecular Mechanics Generalized Born Surface Area; SASA, solvent-accessible surface area; SD, standard deviation; ΔVDWAALS, van der Waals interaction energy; ΔEEL, electrostatic interaction energy; ΔEGB, polar solvation free energy (Generalized Born model); ΔESURF, nonpolar (SASA-based) solvation free energy; ΔGGAS, gas-phase energy (ΔVDWAALS + ΔEEL); ΔGSOLV, total solvation free energy (ΔEGB + ΔESURF); ΔTOTAL, total binding free energy (ΔGGAS + ΔGSOLV). Rep1–Rep3, biological replicates 1–3. All values were calculated with the MM/GBSA method (igb = 5, 0.15 M salt concentration) implemented in gmx_MMPBSA [25].

Van der Waals interactions contributed favorably and consistently, with a mean value of −69.64 ± 10.98 kcal/mol. Electrostatic interactions were strongly favorable (−1004.14 ± 207.39 kcal/mol) but were largely offset by the unfavorable polar-solvation contribution (1026.26 ± 205.48 kcal/mol). The nonpolar-solvation term remained favorable in all three simulations, with a mean of −10.65 ± 1.67 kcal/mol. Together, these components resulted in favorable calculated total binding energies across the three independent trajectories.

3.6. Recurrent Contacts and Energetic Hotspots Define the Interface

Residue-pair analysis using a 0.60-nm heavy-atom cutoff identified two contacts present in all three simulations (Table 2). (Arg128) TmGpx1—(Trp12) CK2β showed a mean contact frequency of 98.47 ± 2.42% and a mean minimum distance of 0.3595 nm. (Val126) TmGpx1—(Glu73) CK2β showed a mean contact frequency of 86.05 ± 15.16% and a mean minimum distance of 0.4630 nm.

Table 2. Persistent CK2β–TmGpx1 residue contacts identified across the three MD replicates. Contact frequency, minimum distance, replicate occurrence, and mean per-residue binding free-energy contributions are shown. Highlights indicate the two contact pairs conserved across all three replicates (yellow) and contacts involving the TmGpx1 catalytic-triad residue Trp131 (green).

Contact Rank	CK2β _ Residue	TmGpx1_ Residue	Mean ± SD_ Contact_ freq_%	mean_ min_dist_ nm	n_replicates	CK2β_ΔG_mean	TmGpx1_ΔG_mean
1	TRP:12	ARG:128	98.47 ± 2.42	0.3595	3	−3.37	−6.03
2	GLU:73	VAL:126	86.05 ± 15.16	0.463	3	−1.83	−1.89
3	LEU:62	ILE:151	99.87 ± 0.06	0.3959	2	−0.63	−3.27
4	TRP:12	VAL:126	99.32 ± 0.71	0.4052	2	−3.37	−1.89
5	GLU:57	TRP:131	98.9 ± 1.42	0.3605	2	−0.10	−3.62
6	GLU:63	ILE:151	98.82 ± 1.23	0.3902	2	0.11	−3.27

Table 2. *Cont.*

Contact Rank	CK2β _ Residue	TmGpx1_ Residue	Mean ± SD_ Contact_ freq_%	mean_ min_dist_ nm	n_replicates	CK2β_ΔG_mean	TmGpx1_ΔG_mean
7	GLU:5	GLY:106	98.4 ± 0.58	0.3284	2	−1.77†	−2.17‡
8	TRP:9	ARG:128	97.95 ± 2.9	0.3712	2	−1.64	−6.03
9	PRO:58	TRP:131	97.73 ± 1.81	0.3684	2	−1.59	−3.62
10	GLU:73	ARG:149	97.66 ± 0.27	0.3142	2	−1.83	−7.44
11	VAL:7	ARG:128	97.15 ± 3.8	0.3114	2	−0.87†	−6.03
12	SER:69	ILE:151	97.1 ± 3.87	0.4007	2	−0.50	−3.27
13	MET:52	LEU:130	97.08 ± 3.99	0.3966	2	−0.56	−2.19
14	GLU:5	ASN:105	96.67 ± 1.8	0.3656	2	−1.77†	−1.75‡
15	LEU:56	TRP:131	96.66 ± 4.06	0.388	2	−0.17†	−3.62
16	SER:69	ARG:149	96.57 ± 4.48	0.37	2	−0.50	−7.44
17	GLU:57	GLN:76	96.46 ± 4.58	0.3308	2	−0.10	−2.10†
18	ASP:70	ARG:149	96.35 ± 2.38	0.3414	2	−0.63	−7.44
19	SER:8	ARG:128	95.43 ± 5.55	0.4277	2	0.06‡	−6.03
20	GLU:6	ASN:105	93.59 ± 5.81	0.4292	2	−1.23	−1.75‡
21	GLU:6	GLY:106	93.4 ± 8.06	0.3745	2	−1.23	−2.17‡
22	ASP:55	TRP:131	92.52 ± 9.41	0.4236	2	0.41	−3.62
23	GLN:74	LEU:123	90.33 ± 7.95	0.3881	2	−0.22†	−2.02

Abbreviations: MM/GBSA, Molecular Mechanics Generalized Born Surface Area; SD, standard deviation; CK2β residue / TmGpx1 residue, three-letter amino-acid code and residue number for the contacting side chain on each protein; Mean±SD contact freq (%), mean ± SD percentage of trajectory frames (across the replicates in which the pair met the ≥30% threshold) in which the residue pair was within the 0.60 nm heavy-atom contact cutoff; Mean min. dist. (nm), mean minimum heavy-atom distance between the residue pair; n replicates, number of the three replicates in which the contact met the ≥30% frequency threshold; CK2β ΔG mean / TmGpx1 ΔG mean, per-residue MM/GBSA binding free-energy contribution (kcal/mol) of each residue, representing the total contribution of that residue to binding rather than a pair-specific interaction energy, averaged across the three replicates. †, residue present in the decomposition output of two replicates; ‡, residue present in one replicate (mean of available replicates). The table lists all pairs present in all three replicates, regardless of mean contact frequency, and pairs present in two replicates with a mean contact frequency ≥90%. Contact pairs are ordered first by n replicates (n = 3 before n = 2) and then in descending order of mean contact frequency.

Several additional contacts recurred in two of the three simulations, showing that the interface was distributed across multiple residues rather than dominated by a single pair (Table 2; complete replicate-specific networks in Supplementary Table S6A–C). Notably, TmGpx1 Val126, Leu123, and Leu124—residues previously identified at the TmGpx1–FKBP15 interface [14]—also recurred as CK2β contact partners here. Additionally, (Val126) TmGpx1—(Trp12) CK2β was observed in two replicates (99.32 ± 0.71%); (Leu123) TmGpx1—(Gln74) CK2β was observed in two replicates (90.33 ± 7.95%); together with the (Leu123) TmGpx1—(Arg17) CK2β hydrogen bond described in Section 3.3, this indicates that Leu123 engages more than one CK2β residue at the interface; and (Leu124) TmGpx1 formed high-frequency contacts with several CK2β residues in Replicate 3 (e.g., (Leu124) TmGpx1—(Ser69) CK2β at 99.45%), consistent with the hydrogen bond reported in Section 3.3.

The contact analysis also identified the TmGpx1 active-site residues Cys39, Gln76, and Trp131 among the recurring CK2β contact partners. (Gln76)TmGpx1—(Glu57)CK2β was present in two replicates (96.46 ± 4.58%) and corresponded to the hydrogen bond described in Section 3.3; (Cys39)TmGpx1—(Glu57)CK2β was identified in two replicates (Replicate 1: 93.78%; Replicate 2: 43.20%; Supplementary Table S6A,B); and Trp131 formed high-frequency contacts with multiple CK2β residues across all three replicates—such as (Glu57)CK2β, (Pro58)CK2β, (Leu56)CK2β, (Asp55)CK2β, (Trp12)CK2β, (Leu16)CK2β, and (Gly15)CK2β. (Table 2; Supplementary Table S6A–C).

Visualization of the Replicate 1 dominant-cluster structure confirmed the spatial proximity of the two contact pairs observed in all three replicates, with closest heavy-atom distances of 3.16 Å for (Arg128) TmGpx1—(Trp12) CK2β and 4.25 Å for (Val126) TmGpx1—(Glu73) CK2β (Figure 4).

Per-residue MM/GBSA decomposition identified five CK2β residues and ten TmGpx1 residues with a mean ΔG contribution of ≤ −1.0 kcal/mol across the three replicates (Figure 5). The selected CK2β residues included Trp12, Glu73, Trp9, Pro58, and Glu6, whereas the TmGpx1 set included Arg149, Arg128, Trp131, Ile151, Leu124, Leu130, Lys153, Leu123, Val126, and Phe41. The overlap between the contact-frequency and energetic-

decomposition analyses, particularly for (Arg128) TmGpx1—(Trp12) CK2β and (Val126) TmGpx1—(Glu73) CK2β, supports a reproducible but distributed interaction interface.

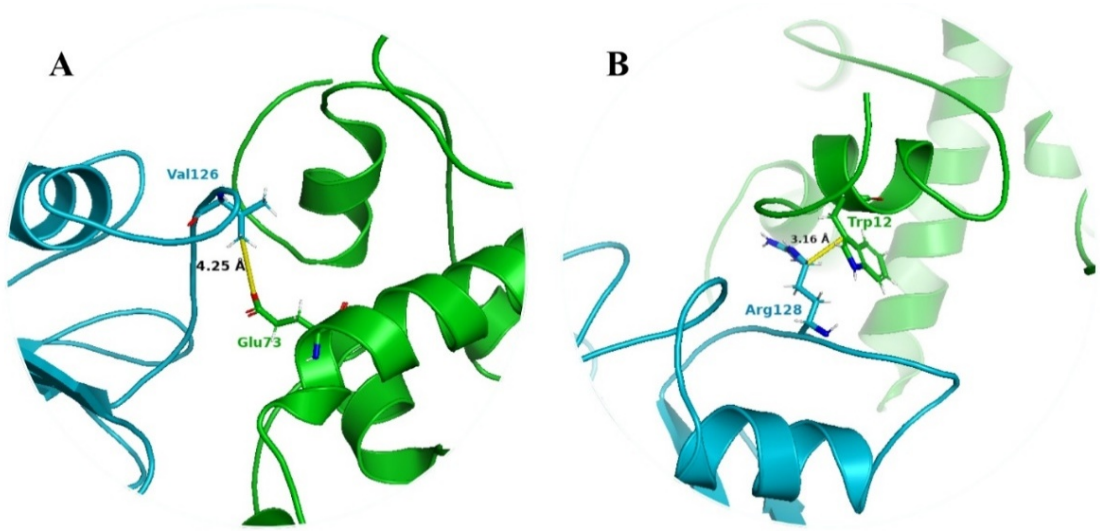


Figure 4. Representative interfacial contacts in the TmGpx1–CK2β complex. The dominant Cluster 1 structure from Replicate 1 is shown with CK2β in green and TmGpx1 in cyan. (**A**) CK2β Glu73–TmGpx1 Val126 contact (4.25 Å). (**B**) CK2β Trp12–TmGpx1 Arg128 contact (3.16 Å). Both contact pairs were consistently observed across all three simulation replicates.

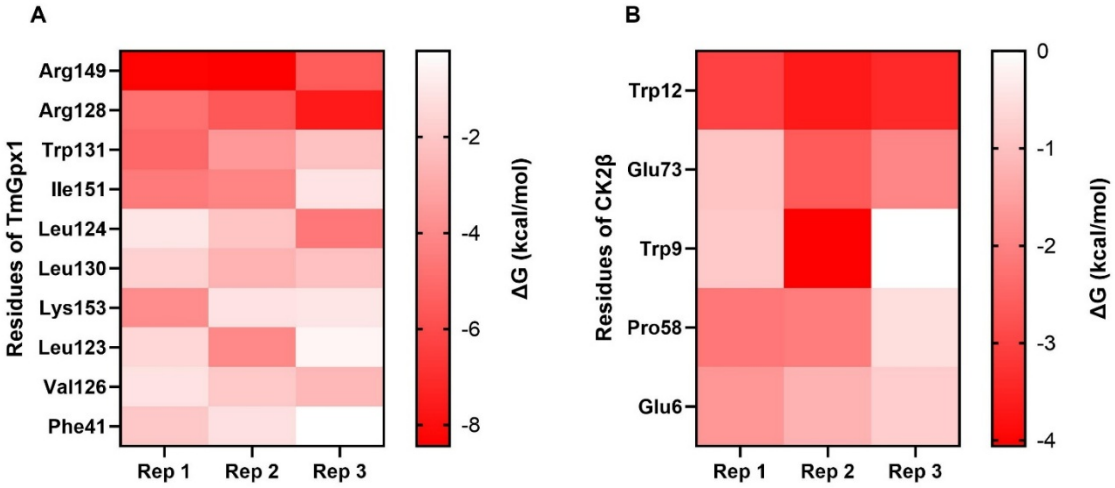


Figure 5. Per-residue binding free-energy contributions of CK2β and TmGpx1 across three independent molecular dynamics simulations. Heatmaps show the mean per-residue binding free-energy contribution (ΔG) obtained from MM/GBSA (Molecular Mechanics Generalized Born Surface Area) decomposition of 201 frames from each replicate for (**A**) TmGpx1 and (**B**) CK2β. Only residues present in the decomposition outputs of all three replicates were evaluated. Residues were classified as energetically significant interface residues when their mean ΔG across the three replicate-level values was ≤ −1.0 kcal/mol; five CK2β residues and ten TmGpx1 residues met this criterion. More negative values, indicated by darker red shading, represent more favorable calculated contributions to complex formation, whereas lighter shading indicates weaker contributions.

4. Discussion

CK2β is the non-catalytic regulatory subunit of the CK2 holoenzyme and contributes to holoenzyme organization, substrate selection, and protein recruitment. It also participates in CK2-associated and CK2-independent scaffolding functions linked to cytoskeletal organization [15–18]. Structurally, CK2β contains a conserved zinc-binding region that supports β-subunit dimerization and a C-terminal region that participates in

association with the catalytic subunits, allowing the CK2β dimer to serve as a central scaffold for holoenzyme assembly [16]. Direct binding of a pathogen protein to CK2β, with a defined functional consequence, has already been demonstrated: the Epstein-Barr virus protein EBNA1 binds CK2β directly through a defined internal sequence, and this interaction recruits the CK2 holoenzyme to promyelocytic leukemia (PML) nuclear bodies, increasing CK2-mediated phosphorylation of PML and triggering its degradation [26]. This binding occurs at a specific KSSR motif near the CK2β dimerization interface, a docking site also used by an unrelated cellular protein, ARKL1, indicating that CK2β can serve as a reusable interaction surface for structurally distinct binding partners [27]. Separately, vaccinia virus requires host CK2 activity for efficient actin-tail formation and cell-to-cell spread, providing additional precedent for CK2-dependent signaling being exploited during infection [28]. CK2 hijacking is not limited to these two examples: several additional Epstein–Barr virus proteins (EBNA2, LMP1, ZEBRA, EB-2) are themselves direct CK2 substrates, and the unrelated retroviral oncoprotein HTLV-1 Tax is likewise phosphorylated by CK2 at a site adjacent to its PDZ-binding motif, indicating that engagement of the CK2 holoenzyme is a repeatedly exploited strategy among otherwise unrelated pathogens [29,30]. Together, these studies establish that CK2β is both a validated direct target of pathogen proteins and a hub capable of accommodating multiple, unrelated interaction partners.

In the present study, the predicted TmGpx1–CK2β complex underwent conformational rearrangement while maintaining a persistent interaction interface across independent simulations. The continued association was supported by complementary measurements of intermolecular proximity, atomic contacts, hydrogen bonding, interfacial burial, salt bridges, conformational clustering, and end-state binding-energy estimates, indicating that the Y2H-identified interaction is structurally compatible under the simulated conditions.

The TmGpx1-facing region identified here (CK2β residues 1–73) is spatially distinct from the KSSR motif (residues ~147–150) that mediates the EBNA1 and ARKL1 interactions described above. TmGpx1 therefore appears to engage a different surface of CK2β than the one already characterized for these other partners, rather than competing with a known docking site. Because CK2β functions as a regulatory docking platform, association with TmGpx1 at this distinct surface could plausibly influence the recruitment of CK2β-interacting proteins or the accessibility of selected substrate-binding surfaces, drawing on the same general principle—CK2β-mediated redirection of the holoenzyme toward specific outcomes—already established for EBNA1. This possibility is reinforced by the established, non-redundant contribution of CK2β to cytoskeletal organization: CK2 localizes to microtubule-containing structures such as the mitotic spindle and promotes microtubule assembly and stability through mechanisms that do not depend exclusively on catalytic activity, and genetic deletion of CK2β alone—independent of the catalytic subunits—impairs tubulin polymerization and destabilizes microtubule organization [17–20]. Such an effect could in turn alter CK2-associated signaling pathways relevant to cytoskeletal organization, membrane trafficking, or macrophage responses, offering a structural basis by which TmGpx1 could influence host processes relevant to the intracellular survival of *T. marneffei*.

Comparison with our previous TmGpx1–FKBP15 study revealed a recurrent TmGpx1 interface region. Pro121, Leu123, Leu124, Val126, and Lys127 were previously implicated in the FKBP15 interaction, whereas Leu123, Leu124, and Val126 also participated in the predicted CK2β interface in the present study [14]. Val126 formed reproducible contacts with CK2β, while Leu123 and Leu124 participated in residue contacts or hydrogen bonds with CK2β residues. The repeated involvement of this region with two structurally and functionally distinct host proteins indicates that residues surrounding Leu123–Val126 constitute a reusable host-protein-binding surface on TmGpx1.

TmGpx1 is canonically associated with peroxide reduction and antioxidant defense, and its Y2H-supported interactions with both FKBP15 and CK2β through this shared surface support the hypothesis that TmGpx1 functions as a moonlighting protein, possessing an additional capacity to engage human regulatory proteins beyond its enzymatic role. Reuse of a single interface across two structurally and functionally unrelated host partners is a recognized structural signature of moonlighting behavior, consistent with TmGpx1 acting as a hub for host-protein engagement during infection.

This mode of moonlighting is not unique to TmGpx1 among fungal pathogens. In *Candida albicans* and *Nakaseomyces glabratus* (formerly *Candida glabrata*), the glycolytic enzyme glyceraldehyde-3-phosphate dehydrogenase (GAPDH)—like TmGpx1, a cytosolic metabolic enzyme with no classical secretion signal—is additionally found at the cell surface, where it binds the human proteins vitronectin and plasminogen with high affinity by docking onto the fungal adhesins Als3 and Epa6 to promote host attachment [31]. Similarly, the *C. albicans* peroxiredoxin Tsa1p, an antioxidant enzyme of the same thiol-peroxidase superfamily as glutathione peroxidases, has an established secondary role in fungal cell wall biogenesis beyond its canonical oxidative-stress function [32]. These precedents indicate that redox and metabolic enzymes are recurrently repurposed for host-

facing or structural roles in fungal pathogens, lending independent support to the hypothesis that TmGpx1 similarly moonlights as a host-protein-binding factor during *T. marneffei* infection.

This study has some limitations. The TmGpx1–CK2β interaction identified here is based on yeast two-hybrid screening and computational modeling; no direct biophysical or cellular assay has yet confirmed this association under physiological conditions or measured its effect on CK2 signaling, cytoskeletal organization, or fungal survival. MM/GBSA values should likewise be interpreted as comparative energetic estimates rather than experimentally measured binding affinities. Future work should prioritize site-directed mutagenesis of the shared TmGpx1 hotspot residues (e.g., Leu124, Val126, Arg128) and the catalytic triad, paired with binding assays such as co-immunoprecipitation, surface plasmon resonance, or biolayer interferometry, together with CK2 kinase activity assays, to determine whether this interaction occurs in host cells and modulates CK2-associated signaling during *T. marneffei* infection.

In conclusion, this study provides structural evidence for a persistent, energetically favorable interaction between TmGpx1 and CK2β, supported by recurrent contacts involving TmGpx1 Arg128 and Val126 and CK2β Trp12 and Glu73. The overlap between this CK2β-facing region and the Leu123–Leu124–Val126 surface previously implicated in FKBP15 binding, together with the involvement of TmGpx1's Cys39/Gln76/Trp131 catalytic triad, supports the hypothesis that TmGpx1 functions as a moonlighting protein, engaging host regulatory proteins through a reusable interface that may be coupled to its own catalytic function. That pathogen proteins can directly bind CK2β to redirect host regulatory outcomes is an established phenomenon in an unrelated system [26,27], lending further plausibility to this model. Biochemical and cellular validation will be needed to confirm the interaction and determine its relevance to *T. marneffei* pathogenesis. Taken together, this work broadens our understanding of the molecular mechanisms underlying host–pathogen interactions and lays a foundation for future studies to uncover how *T. marneffei* and other fungal pathogens exploit host signaling networks to support intracellular survival.

Supplementary Materials

The additional data and information can be downloaded at: https://media.sciltp.com/articles/others/26101913 55411601/eMicrobe-26080001-SI.pdf. Supplementary Data 1: Input sequences for AlphaFold analysis. Supplementary Data 2: AlphaFold 3 confidence metrics for the predicted TmGpx1–CK2β complex models. Supplementary Tables S1–S6 and description. Supplementary Figures S1–S3 and Figure legends.

Author Contributions

Y.H.H.O. conducted the molecular dynamics simulations and prepared the figures and tables. T.W. and M.P. conceived and supervised the study. Data analysis was performed jointly by Y.H.H.O., N.L., T.W. and M.P. Y.H.H.O. prepared the original manuscript draft. M.P. reviewed, revised, and finalized the manuscript. All authors have read and approved the final version of the manuscript.

Funding

This study was supported by the Faculty of Medicine Research Fund, and Fundamental Fund 2568 (Grant no. 4773384), Chiang Mai University and Thailand Science Research and Innovation (TSRI) (FRB680102/0162) to M.P. Y.H.H.O. graduate study was support by an overseas fund, Faculty of Medicine, Chiang Mai University. The authors gratefully acknowledge the ERAWAN high-performance computing facility and the Information Technology Service Center (ITSC), Chiang Mai University, for providing computational resources and technical support.

Institutional Review Board Statement

Not applicable.

Informed Consent Statement

Not applicable.

Data Availability Statement

All data supporting the findings of this study are included in this article and its Supplementary Materials.

Conflicts of Interest

The authors declare no conflict of interest.

Use of AI and AI-Assisted Technologies

The three-dimensional structure of the TmGpx1–CK2β complex was predicted using AlphaFold 3, accessed via the AlphaFold Server, and the top-ranked model, selected on the basis of its ranking score together with pTM and ipTM confidence metrics, served as the initial structure for the molecular dynamics simulations. All predicted models and subsequent outputs were critically assessed by the authors, who take full responsibility for the content of this article.

References

1. Pruksaphon, K.; Nosanchuk, J.D.; Ratanabanangkoon, K.; et al. Talaromyces Marneffei Infection: Virulence, Intracellular Lifestyle and Host Defense Mechanisms. *J. Fungi* **2022**, *8*, 200. https://doi.org/10.3390/jof8020200.
2. Narayanasamy, S.; Dougherty, J.; van Doorn, H.R.; et al. Pulmonary Talaromycosis: A Window into the Immunopathogenesis of an Endemic Mycosis. *Mycopathologia* **2021**, *186*, 707–715. https://doi.org/10.1007/s11046-021-00570-0.
3. Pasricha, S.; MacRae, J.I.; Chua, H.H.; et al. Extensive Metabolic Remodeling Differentiates Non-Pathogenic and Pathogenic Growth Forms of the Dimorphic Pathogen Talaromyces Marneffei. *Front. Cell. Infect. Microbiol.* **2017**, *7*, 368. https://doi.org/10.3389/fcimb.2017.00368.
4. Cogliati, M.; Roverselli, A.; Boelaert, J.R.; et al. Development of an in Vitro Macrophage System to Assess Penicillium Marneffei Growth and Susceptibility to Nitric Oxide. *Infect. Immun.* **1997**, *65*, 279–284. https://doi.org/10.1128/iai.65.1.279-284.1997.
5. Pongpom, M.; Vanittanakom, P.; Nimmanee, P.; et al. Adaptation to Macrophage Killing by *Talaromyces marneffei*. *Future Sci. OA* **2017**, *3*, FSO215. https://doi.org/10.4155/fsoa-2017-0032.
6. Ellett, F.; Pazhakh, V.; Pase, L.; et al. Macrophages Protect Talaromyces Marneffei Conidia from Myeloperoxidase-Dependent Neutrophil Fungicidal Activity during Infection Establishment in Vivo. *PLOS Pathog.* **2018**, *14*, e1007063. https://doi.org/10.1371/journal.ppat.1007063.
7. Tiwari, S.; Thakur, R.; Shankar, J. Role of Heat-Shock Proteins in Cellular Function and in the Biology of Fungi. *Biotechnol. Res. Int.* **2015**, *2015*, 132635. https://doi.org/10.1155/2015/132635.
8. Payne, M.; Weerasinghe, H.; Tedja, I.; et al. A Unique Aspartyl Protease Gene Expansion in *Talaromyces marneffei* Plays a Role in Growth inside Host Phagocytes. *Virulence* **2019**, *10*, 277–291. https://doi.org/10.1080/21505594.2019.1593776.
9. Wangsanut, T.; Amsri, A.; Pongpom, M. Antibody Screening Reveals Antigenic Proteins Involved in Talaromyces Marneffei and Human Interaction. *Front. Cell. Infect. Microbiol.* **2023**, *13*, 1118979. https://doi.org/10.3389/fcimb.2023.1118979.
10. Pongpom, M.; Vanittanakom, N. Stress Adaptation in Talaromyces Marneffei. *Chiang Mai Med. J.* **2016**, *55*, 23–30. https://doi.org/10.14456/cmmj.2016.3.
11. Yang, B.; Wang, J.; Jiang, H.; et al. Extracellular Vesicles Derived from Talaromyces Marneffei Yeasts Mediate Inflammatory Response in Macrophage Cells by Bioactive Protein Components. *Front. Microbiol.* **2021**, *11*, 603183. https://doi.org/10.3389/fmicb.2020.603183.
12. Coschigano, P.W.; Magasanik, B. The *URE2* Gene Product of *Saccharomyces cerevisiae* Plays an Important Role in the Cellular Response to the Nitrogen Source and Has Homology to Glutathione *S*-Transferases. *Mol. Cell. Biol.* **1991**, *11*, 822–832. https://doi.org/10.1128/mcb.11.2.822-832.1991.
13. Karkowska-Kuleta, J.; Kozik, A. Moonlighting Proteins as Virulence Factors of Pathogenic Fungi, Parasitic Protozoa and Multicellular Parasites. *Mol. Oral Microbiol.* **2014**, *29*, 270–283. https://doi.org/10.1111/omi.12078.
14. Wangsanut, T.; Aung, Y.H.H.; Oo, Y.H.H.; et al. Glutathione Peroxidase from Talaromyces Marneffei Interacts with Host Cytoskeletal Proteins: Insights from Yeast Two-Hybrid and Molecular Dynamics Simulations. *Int. J. Mol. Sci.* **2026**, *27*, 4259. https://doi.org/10.3390/ijms27104259.
15. Litchfield, D.W. Protein Kinase CK2: Structure, Regulation and Role in Cellular Decisions of Life and Death. *Biochem. J.* **2003**, *369*, 1–15. https://doi.org/10.1042/bj20021469.
16. Chantalat, L.; Leroy, D.; Filhol, O.; et al. Crystallization and Preliminary X-Ray Diffraction Analysis of the Regulatory Subunit of Human Protein Kinase CK2. *Acta Crystallogr. Sect. D Biol. Crystallogr.* **1999**, *55*, 895–897. https://doi.org/10.1107/s0907444998016680.
17. Canton, D.A.; Litchfield, D.W. The Shape of Things to Come: An Emerging Role for Protein Kinase CK2 in the Regulation of Cell Morphology and the Cytoskeleton. *Cell. Signal.* **2006**, *18*, 267–275. https://doi.org/10.1016/j.cellsig.2005.07.008.

18. D'Amore, C.; Salizzato, V.; Borgo, C.; et al. A Journey through the Cytoskeleton with Protein Kinase CK2. *Curr. Protein Pept. Sci.* **2019**, *20*, 547–562. https://doi.org/10.2174/1389203720666190119124846.
19. Lim, A.C.B.; Tiu, S.Y.; Li, Q.; et al. Direct Regulation of Microtubule Dynamics by Protein Kinase CK2. *J. Biol. Chem.* **2004**, *279*, 4433–4439. https://doi.org/10.1074/jbc.m310563200.
20. Münzer, P.; Walker-Allgaier, B.; Geue, S.; et al. CK2β Regulates Thrombopoiesis and Ca2+-Triggered Platelet Activation in Arterial Thrombosis. *Blood* **2017**, *130*, 2774–2785. https://doi.org/10.1182/blood-2017-05-784413.
21. Larson, S.R.; Bortell, N.; Illies, A.; et al. Myeloid Cell CK2 Regulates Inflammation and Resistance to Bacterial Infection. *Front. Immunol.* **2020**, *11*, 590266. https://doi.org/10.3389/fimmu.2020.590266.
22. Abramson, J.; Adler, J.; Dunger, J.; et al. Accurate Structure Prediction of Biomolecular Interactions with AlphaFold 3. *Nature* **2024**, *630*, 493–500. https://doi.org/10.1038/s41586-024-07487-w.
23. Krokidis, M.G.; Koumadorakis, D.E.; Lazaros, K.; et al. AlphaFold3: An Overview of Applications and Performance Insights. *Int. J. Mol. Sci.* **2025**, *26*, 3671. https://doi.org/10.3390/ijms26083671.
24. Lobanov, M.Y.; Bogatyreva, N.S.; Galzitskaya, O.V. Radius of Gyration as an Indicator of Protein Structure Compactness. *Mol. Biol.* **2008**, *42*, 623–628. https://doi.org/10.1134/s0026893308040195.
25. Valdés-Tresanco, M.S.; Valdés-Tresanco, M.E.; Valiente, P.A.; et al. gmx_MMPBSA: A New Tool to Perform End-State Free Energy Calculations with GROMACS. *J. Chem. Theory Comput.* **2021**, *17*, 6281–6291. https://doi.org/10.1021/acs.jctc.1c00645.
26. Sivachandran, N.; Cao, J.Y.; Frappier, L. Epstein-Barr Virus Nuclear Antigen 1 Hijacks the Host Kinase CK2 to Disrupt PML Nuclear Bodies. *J. Virol.* **2010**, *84*, 11113–11123. https://doi.org/10.1128/jvi.01183-10.
27. Cao, J.Y.; Shire, K.; Landry, C.; et al. Identification of a Novel Protein Interaction Motif in the Regulatory Subunit of Casein Kinase 2. *Mol. Cell. Biol.* **2014**, *34*, 246–258. https://doi.org/10.1128/mcb.00968-13.
28. Alvarez, D.E.; Agaisse, H. Casein Kinase 2 Regulates Vaccinia Virus Actin Tail Formation. *Virology* **2012**, *423*, 143–151. https://doi.org/10.1016/j.virol.2011.12.003.
29. Montenarh, M.; Grässer, F.A.; Götz, C. Protein Kinase CK2 and Epstein–Barr Virus. *Biomedicines* **2023**, *11*, 358. https://doi.org/10.3390/biomedicines11020358.
30. Bidoia, C.; Mazzorana, M.; Pagano, M.A.; et al. The Pleiotropic Protein Kinase CK2 Phosphorylates HTLV-1 Tax Protein in Vitro, Targeting Its PDZ-Binding Motif. *Virus Genes* **2010**, *41*, 149–157. https://doi.org/10.1007/s11262-010-0494-3.
31. Bednarek, A.; Satala, D.; Zawrotniak, M.; et al. Glyceraldehyde 3-Phosphate Dehydrogenase on the Surface of Candida Albicans and Nakaseomyces Glabratus Cells—a Moonlighting Protein that Binds Human Vitronectin and Plasminogen and Can Adsorb to Pathogenic Fungal Cells via Major Adhesins Als3 and Epa6. *Int. J. Mol. Sci.* **2024**, *25*, 1013. https://doi.org/10.3390/ijms25021013.
32. Urban, C.; Xiong, X.; Sohn, K.; et al. The Moonlighting Protein Tsa1p Is Implicated in Oxidative Stress Response and in Cell Wall Biogenesis in *Candida albicans*. *Mol. Microbiol.* **2005**, *57*, 1318–1341. https://doi.org/10.1111/j.1365-2958.2005.04771.x.